

Reversible strain in Ni-Mn-Ga with collinear field and stress

LeAnn E. Faidley,^a Marcelo J. Dapino,^a Gregory N. Washington,^a Thomas A. Lograsso^b

^a Department of Mechanical Engineering, The Ohio State University, Columbus, OH, 43202

^b U.S. Department of Energy & Iowa State University, Ames, IA, 50011

ABSTRACT

Our previous work on ferromagnetic shape memory $\text{Ni}_{50}\text{Mn}_{28.7}\text{Ga}_{21.3}$ demonstrates reversible compressive strains of $\epsilon = -4100\mu\epsilon$ along the [001] direction under the application of a magnetic field also along the [001] direction with no external orthogonal restoring force. The reversibility of the strains is due to internal bias stresses oriented orthogonal to the field. These results show promise for the use of Ni-Mn-Ga as the core material in solenoid transducers. In this paper, the reversible strains are explained by considering pinning sites as the source of the internal bias stresses in the material. Following prior work by Kiefer and Lagoudas,¹ a phenomenological model is constructed for the motion of twin variants in the presence of an orthogonal pair formed by a magnetic field and an internal bias stress. The model is formulated by considering the Zeeman, elastic, and pinning energies, from which an appropriate Gibbs energy function is constructed. Minimization of the Gibbs function then yields a constitutive model for the strain. The accuracy of this model is studied and its implementation as a hysteresis kernel in homogenization theories is discussed.

1. INTRODUCTION AND MOTIVATION

Ferromagnetic shape memory nickel-manganese-gallium (Ni-Mn-Ga) is attractive for transducer applications due to the fact that it exhibits strains of 6^{2,3} to 9.5%⁴ when exposed to magnetic fields of 400 kA/m. Such strains are on the order of those possible from shape memory alloys (SMAs) but because they are generated in response to magnetic fields a higher frequency bandwidth is possible.⁵ As with standard SMAs, the large strains in Ni-Mn-Ga originate in the pseudo-elasticity that occurs due to the reorientation of the martensitic twin variants. In ferromagnetic shape memory alloys (FSMAs), however, the reorientation can be driven by magnetic fields or external stresses. Unlike standard SMAs, Ni-Mn-Ga is typically employed solely in its low temperature martensitic phase and hence lacks the restoring mechanism that the phase transformation in SMAs provides. Thus, in order to achieve giant strains from Ni-Mn-Ga, an external force needs to be applied orthogonal to the applied field to restore the original orientation of the twin variants. Our tests have shown that reversible strains of -0.41%, which is over a two-fold strain increase over Terfenol-D, are achievable in $\text{Ni}_{50}\text{Mn}_{28.7}\text{Ga}_{21.3}$ when the applied field and output strain are along [001] and no external restoring force is applied. Existing models for twin variant reorientation in Ni-Mn-Ga cannot predict such reversible strains. This paper, therefore, provides an additional component to the current description of the strain mechanism in $\text{Ni}_{50}\text{Mn}_{28.7}\text{Ga}_{21.3}$ and offers an explanation for both the reversibility and the smaller magnitude of the strain obtained in previous tests.

The strain mechanism for Ni-Mn-Ga is well established in the literature.⁶⁻⁸ As a sample cools from its high temperature austenite phase to its low temperature martensite phase, a self accommodating twinned structure results due to the minimization of the strain energy generated from the mismatch between the cubic and tetragonal lattices. A two-dimensional representation of this twinned structure is shown in Figure 1. At zero field the sample is comprised of two perpendicular variants separated by a twin boundary as illustrated in panel (a). Each variant in turn consists of several distinct magnetic domains which are divided by 180° walls. The twin variant volume fraction and the magnetic domain volume fraction are respectively denoted ξ and α . For reasonably small transverse fields (~ 8 kA/m), all of the magnetization vectors align with the preferred direction of the variant and the magnetic domains disappear as shown in panel (b). Thus it is reasonable to assume $\alpha = 1$.

Further author information: (Send correspondence to M.J.D.)

L.E.F.: E-mail: faidley.1@osu.edu, Telephone: 1-614-688-0361

M.J.D.: E-mail: dapino.1@osu.edu, Telephone: 1-614-688-3689

G.N.W.: E-mail: washington.88@osu.edu, Telephone: 1-614-292-8486

T.A.L.: E-mail: lograsso@ameslab.gov, Telephone: 1-515-294-8727

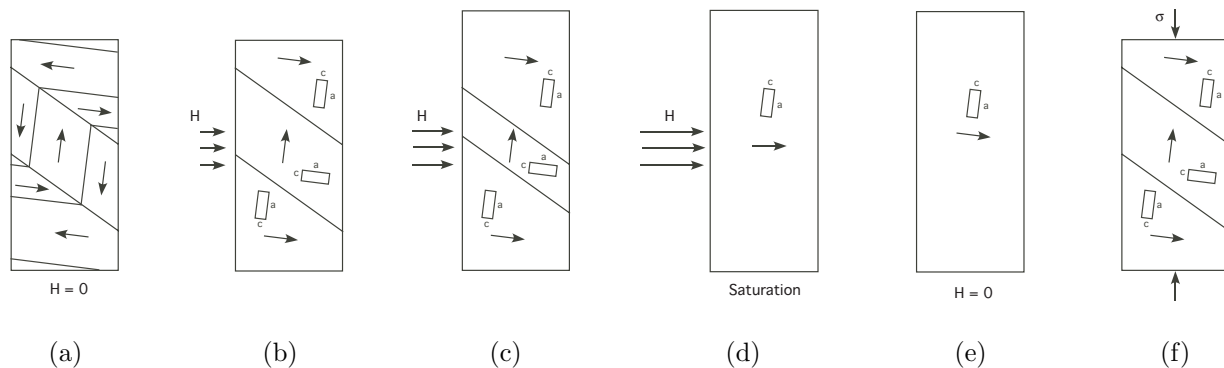


Figure 1. Strain mechanism for FSMAs under orthogonally applied stress and field.

As a transverse field is applied, the variants favored by the field will increase in size through twin reorientation. Ni-Mn-Ga and other FSMAs have large magnetic anisotropy energies compared to the energy necessary to reorient the unit cells at the twin boundary. Thus, as the applied magnetic field attracts the unit cell magnetization vectors towards it, the unit cells along the twin boundary will switch orientation such that their magnetically favored, short c-axis is more closely aligned with the field. This results in the growth of the favored variant at the expense of the other through twin boundary motion and the overall axial lengthening of the sample, as depicted in Figure 1(c). As the field is increased to the point where no further twin boundary motion is possible and the field energy overcomes the magnetic anisotropy energy, the local magnetization vectors break away from the short c-axis and align with the field. This results in magnetic saturation as shown in panel (d). When the field is removed as in panel (e), the magnetic anisotropy energy will restore the local magnetization to the c-axis of the unit cells. Since both variants are equally favorable from an energy standpoint,⁹ there is no restoring force to drive the unit cell reorientation and the size of the sample will not change. Twin boundary motion and reversible strain can be induced by applying an axial field, axial compressive stress, or a transverse tensile stress all of which favor the variant with the short c-axis aligned with the axial direction as is illustrated in panel (f). One common configuration for Ni-Mn-Ga consists of placing a rectangular sample in an electromagnet such that the field is applied transversely and a bias axial compressive stress is always present¹⁰ as depicted in Figure 2.

Research performed at MIT on stoichiometric Ni_2MnGa in the mid 1990s reports reversible compressive strains

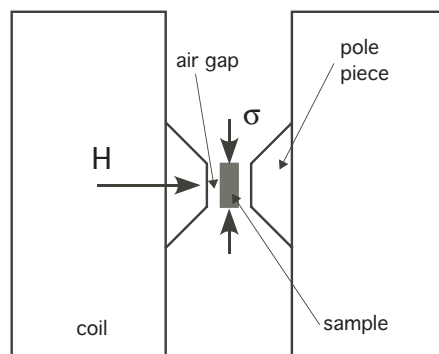


Figure 2. Diagram of field and stress orientations in an electromagnet configuration.

of $\epsilon = -1000\mu\epsilon$ (-0.1%) when the magnetic field is applied along the same direction as the measured strain¹¹ and no restoring force is applied. In previous work¹² we presented results which are reproduced in Figure 3 and show reversible compressive strains of $\epsilon = -4100\mu\epsilon$ (-0.41%) in $\text{Ni}_{50}\text{Mn}_{28.7}\text{Ga}_{21.3}$ with no externally applied restoring force. This is especially relevant because it implies that Ni-Mn-Ga can be employed in a solenoid transducer like that of Figure 4, which can be designed to be smaller, more efficient, and have faster responses than electromagnet transducers which require heavy pole pieces and air gaps. Solenoid transducers are promising for applications in areas such as underwater communications and high bandwidth positioning. In a solenoid transducer the field is applied along the axis of a cylindrical rod and no transverse stress or field is applied. According to the strain mechanism presented in Figure 1 this configuration would not provide reversible strains because of the lack of a restoring mechanism.

We propose a modification to the mechanism described in Figure 1 to include the existence of pinning sites in the martensite which provide an internal restoring force allowing for reversible strain. The pinning sites, which are physically point defects, small regions of a second phase material, or residual stresses can have varying pinning energies.¹⁴ We hypothesize that in our $\text{Ni}_{50}\text{Mn}_{28.7}\text{Ga}_{21.3}$ sample the twin boundaries are pinned to sites which have energies too large to be overcome by the field, represented by circles in Figure 5. When an axial magnetic field is applied, the twin boundaries attempt to displace according to the standard mechanisms for twin variant reorientation as in panel (c) but the field does not provide enough energy to overcome the energy barrier provided by the pinning sites. Instead, the twin boundary displaces as much as possible and as it does work against the pinning sites, energy is dissipated. Saturation is achieved when the field energy is large enough to overcome the anisotropy energy and the magnetic moments align with the field without changing the orientation of the crystal (panel (d)). When the field is removed (panel (e)) the anisotropy energy returns the magnetic moments to the easy c-axis of the crystal and the pinning site energy provides a restoring mechanism for the twin boundary, returning the sample to its original length and magnetization. This theory provides an explanation for the smaller magnitude of strain possible from this sample as well as the reversible strain measured in the absence of an externally applied restoring force.

2. ENERGY FORMULATION FOR FSMAS

The pinning mechanisms discussed in the previous section allow us to drive NiMnGa in a solenoid transducer like that shown in Figure 4. Because this transducer architecture includes a path for flux return, it is more compact and energy efficient than its electromagnet counterpart. To model the strain produced by NiMnGa driven in this manner, a thermodynamics approach similar to that presented by Kiefer and Lagoudas¹ is proposed. An additional term due to internal orthogonal stresses is included in the Gibbs function which quantifies the restoring force found in our experiments. For simplicity, we assume that the structure comprises two variant orientations

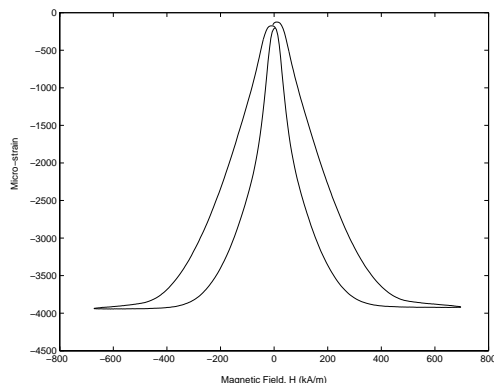


Figure 3. Quasi-static strain output versus input magnetic field for $\text{Ni}_{50}\text{Mn}_{28.7}\text{Ga}_{21.3}$ in a solenoid transducer.¹³

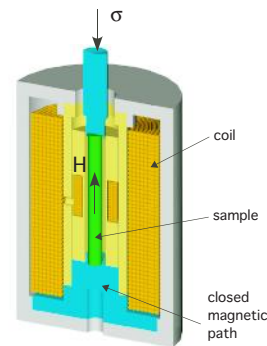


Figure 4. Diagram of field and stress orientations in a solenoid configuration.

described by the two-dimensional representation shown in Figure 6. Variant 2 is defined as that which is favored by an axially applied field in the y-direction and has a volume fraction of ξ . Variant 1 refers to the transverse variant with magnetization vectors oriented in the x-axis and has a volume fraction of $(1 - \xi)$.

The material described in Figure 6 can be treated as a mixture of the two variants. The energy for such a system can be written as

$$G(\boldsymbol{\sigma}, \mathbf{H}, T) = (1 - \xi)G^{V1} + \xi G^{V2} + G^{bound} \quad (1)$$

where G^{Vi} is the energy of the i -th variant and G^{bound} is the energy of the boundary between the two variants. In order to write expressions for G^{Vi} , it is assumed that (a) the system is isothermal and (b) the fields are large enough that the effects of the magnetic domains can be ignored. In this case the expression for the energy of each variant simplifies to the standard expression for Gibbs free energy^{15, 16}

$$G^{Vi}(\boldsymbol{\sigma}, \mathbf{H}, T = \text{const}) = \psi^{Vi} - \frac{1}{2\rho} \boldsymbol{\sigma} \cdot \mathbf{S}^{Vi} \boldsymbol{\sigma} - \frac{\mu_0}{\rho} \mathbf{M}^{Vi} \cdot \mathbf{H} \quad (2)$$

where ψ is the Helmholtz energy, $\boldsymbol{\sigma}$ is the applied stress, \mathbf{S} is the mechanical compliance, \mathbf{M} is the magnetization, \mathbf{H} is the applied field, ρ is the density, and μ_0 is the permeability of free space. Thus, the Gibbs Free Energy of each variant is equal to the Helmholtz energy minus the elastic and Zeeman energy terms.

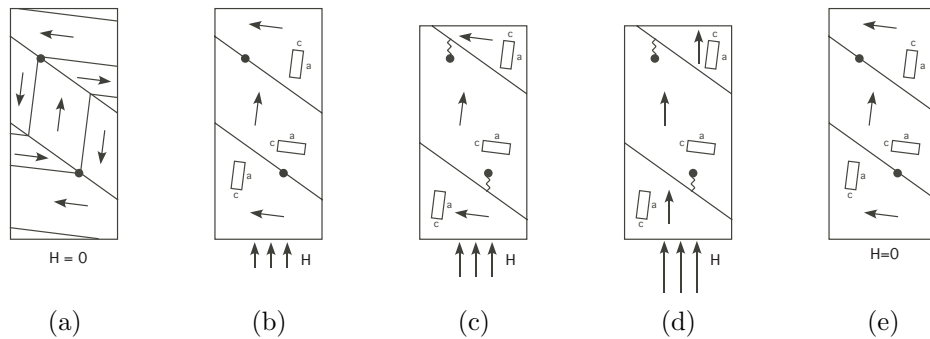


Figure 5. Strain mechanism for FSMA under collinear stress and field. Arrows represent magnetic moments.

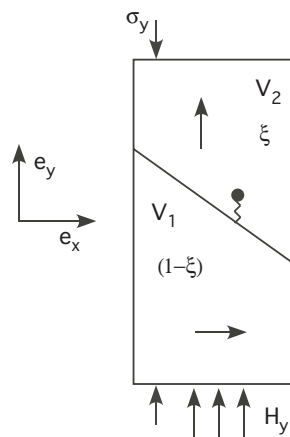


Figure 6. Two-dimensional variants: notation and orientation.

The energy of the twin boundary emanates from two sources. The first is the energy necessary to rotate a unit cell which can be expressed as work done to overcome a force. The second is the energy associated with the pinning sites which act as springs. Thus the boundary energy term has the form

$$G^{bound} = \begin{cases} c_1\xi + k_1\xi^2 & \dot{\xi} > 0 \\ c_2\xi + k_2\xi^2 & \dot{\xi} < 0 \end{cases} \quad (3)$$

where k is the effective spring constant of the pinning sites, c is the force associated with cell reorientation and the two branches of the function occur because the behavior of the material is not the same when the field is increasing and variant 1 is growing as it is when the field is decreasing and variant 1 is shrinking. It is noted that this expression has the same form as the *hardening function* employed by Keifer and Lagoudas¹ on the basis of shape memory arguments.

For the solenoid configuration shown in Figure 4 both the applied stress and applied field are in the axial direction. Using the geometry specified in Figure 6, substitution of (2) and (3) into (1) yields

$$G(\sigma, \mathbf{H}, T = const) = \psi^{V1} - \frac{1}{2\rho} S_{yy}^{V1} \sigma_y^2 + \xi \left[-\frac{1}{2\rho} \Delta S_{yy} \sigma_y^2 - \frac{\mu_0 M_s}{\rho} H_y \right] + \begin{cases} c_1\xi + k_1\xi^2 & \dot{\xi} > 0 \\ c_2\xi + k_2\xi^2 & \dot{\xi} < 0 \end{cases} \quad (4)$$

where the Δ operator refers to the difference between the two variants and $\Delta\psi = 0$ since the Helmholtz energies of the two variants are identical. Having now derived an expression for the free energy, relations can be used to develop expressions for various thermodynamic quantities. The particular relation of interest comes about through the Clausius-Duhem version of the second law of thermodynamics, which states that

$$\pi^\xi = \epsilon_s \sigma_y - \rho \frac{\partial G}{\partial \xi} \quad (5)$$

where $\pi^\xi = \pm Y^\xi$ is the condition for the onset of twin variant motion and ϵ_s is the saturation strain. Differentiation of (4) and substitution into (5) yields the force balance

$$\pm Y^\xi = \epsilon_s \sigma_y - \frac{1}{2} \Delta S_{yy} \sigma_y^2 - \mu_0 M_s H_y - \rho \begin{cases} c_1 + 2k_1\xi & \dot{\xi} > 0 \\ c_2 + 2k_2\xi & \dot{\xi} < 0 \end{cases} \quad (6)$$

Expression (6) can then be solved for our variable of interest, ξ , as

$$\xi = \begin{cases} \frac{1}{2\rho k_1} (\epsilon_s \sigma_y + \frac{1}{2} \Delta S_{yy} \sigma_y^2 + \mu_0 M_s H_y - \rho c_1 - Y^\xi) & \dot{\xi} > 0 \\ \frac{1}{2\rho k_2} (\epsilon_s \sigma_y + \frac{1}{2} \Delta S_{yy} \sigma_y^2 + \mu_0 M_s H_y - \rho c_2 + Y^\xi) & \dot{\xi} < 0 \end{cases} \quad (7)$$

which is dependent on applied field H_y and axial stress σ_y .

3. PARAMETER IDENTIFICATION

In order to determine the volume fraction ξ for varied magnetic field and stress inputs, the parameters k_1 , k_2 , ϵ_s , ΔS_{yy} , M_s , c_1 , c_2 , and Y^ξ in relation (7) need to be determined. Parameters ΔS_{yy} , M_s , and Y^ξ can be measured directly from experiments. For example, M_s is found from the magnetization vs field curve shown in Figure 7. Figure 8 shows the maximum reversible strain possible from the Ni₅₀Mn_{28.7}Ga_{21.3} sample under various applied loads. This data is fit with the expression

$$\epsilon_s = \epsilon_{s,0} \left(\left(\frac{\sigma_y}{\sigma_b} \right)^2 - 2 \left(\frac{\sigma_y}{\sigma_b} \right) + 1 \right) \quad (8)$$

where σ_b is the blocking stress above which very little change occurs in the strain, and $\epsilon_{s,0}$ is the strain possible from an unloaded sample.

The remaining parameters can be found phenomenologically by fitting the desired shape of the hysteresis loop to data for a particular applied stress (σ_p) as shown in Figure 9. The three points indicated in the figure

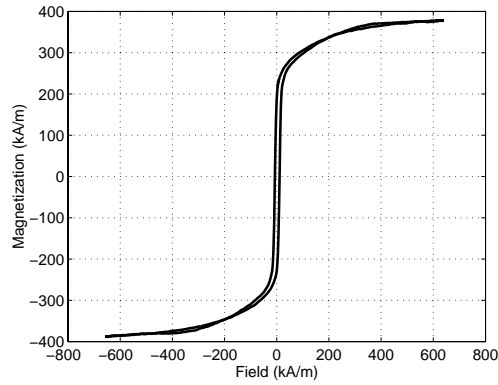


Figure 7. Magnetization vs field curve for $\text{Ni}_{50}\text{Mn}_{28.7}\text{Ga}_{21.3}$.¹³

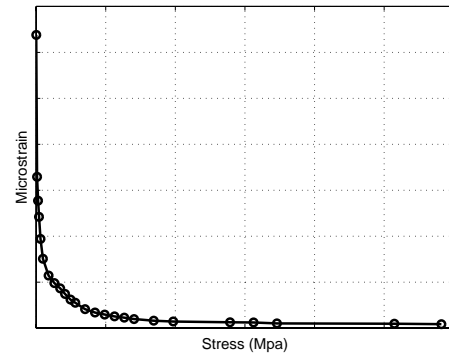


Figure 8. Maximum strain per input axial stress for $\text{Ni}_{50}\text{Mn}_{28.7}\text{Ga}_{21.3}$.¹³

Table 1. Parameters in terms of measured data.

ϵ	$= \xi \epsilon_{th}$
k_1	$= nk_2$
k_2	$= \frac{\mu_0 M_s H_3(\sigma_p) \epsilon_{th}}{2(\epsilon_s(\sigma_p) - \epsilon_2(\sigma_p))}$
c_1	$= \epsilon_s(\sigma_p) \sigma_p + \frac{1}{2} \Delta S_{yy} \sigma_p^2 + \mu_0 M_s H_1(\sigma_p) - Y^\xi(\sigma_p)$
c_2	$= \epsilon_s(\sigma_p) \sigma_p + \frac{1}{2} \Delta S_{yy} \sigma_p^2 + Y^\xi(\sigma_p) - 2k_2 \frac{\epsilon_2(\sigma_p)}{\epsilon_{th}}$
$\epsilon_{s,0}$	$= \frac{\epsilon_s(\sigma_p) \sigma_p^2}{(\sigma_p - \sigma_b)^2}$

yield the following data points (1) field H_1 at the strain turn around point, (2) strain ϵ_2 at the cross over point, (3) field H_3 at the onset of saturation, and (4) saturation strain ϵ_s . Using these measurements the expressions in Table 1 can be used to calculate the parameters needed to implement equation (7).

Note that strain ϵ is related to the volume fraction change ξ through the first equation in Table 1. The maximum theoretical strain for the sample ϵ_{th} occurs if a single twin boundary sweeps through the entire sample thus producing a change in ξ from 0 to 1. Hence, for the case where the boundary is pinned in place, ξ will be limited to a much smaller range.

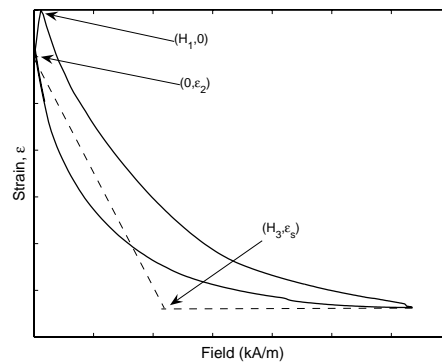


Figure 9. Data points for parameter identification.

4. MODEL RESULTS AND ACCURACY STUDY

To facilitate coding of this model, relation (7) is rewritten as

$$\xi = \begin{cases} \frac{1}{2\rho k_1}(\epsilon_s \sigma_y + \frac{1}{2}\Delta S_{yy}\sigma_y^2 + \mu_0 M_s H_y - \rho c_1 - Y^\xi) & \dot{H} > 0 \text{ and } \xi < \xi_s \\ \xi_s & \xi > \xi_s \\ \frac{1}{2\rho k_2}(\epsilon_s \sigma_y + \frac{1}{2}\Delta S_{yy}\sigma_y^2 + \mu_0 M_s H_y - \rho c_2 + Y^\xi) & \dot{H} < 0 \text{ and } \xi < \xi_s \end{cases} \quad (9)$$

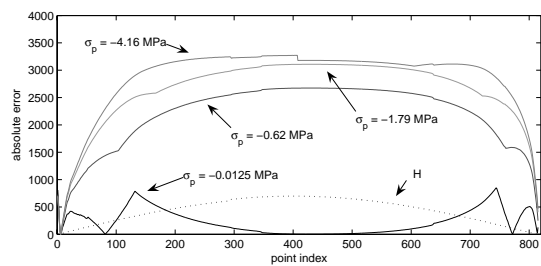
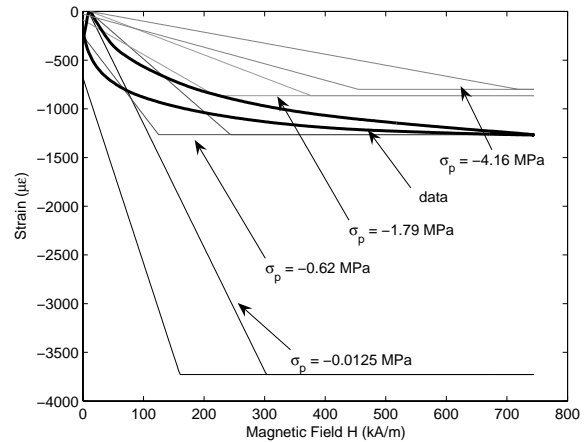
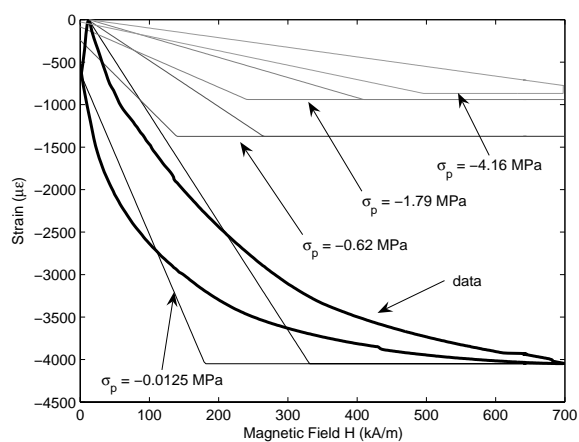
Since this is a phenomenological model and the parameters in these equations are fit to data, we now study the accuracy of the model predictions for a given stress level σ_y if the coefficients are calculated based on various stress levels σ_p . To that end, data points were collected for four stress levels as is shown in Table 2. Each of these sets of data were used to find the coefficients for equation (9) and predictions were made for the strain output at the other three stress levels.

Table 2. Model parameters obtained from measurements collected at various stress values.

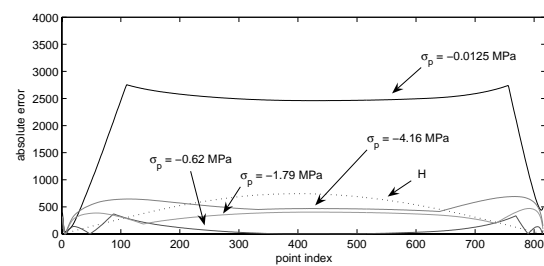
	$\sigma_p = -0.0125$ MPa	$\sigma_p = -0.62$ MPa	$\sigma_p = -1.79$ MPa	$\sigma_p = -4.16$ MPa
ϵ_s ($\mu\epsilon$)	-4050	-1265	-730	-455
H_1 (kA/m)	12	10	11	10
ϵ_2 ($\mu\epsilon$)	-625	-250	-180	-250
H_3 (kA/m)	180	125	180	250

The results are shown in Figure 10, where each graph shows the data and four predictions of the strain for a sinusoidal input field at a particular applied stress σ_y . The four predictions are generated based on the data for various σ_p . Also plotted is the absolute value of the error e between the predicted and the measured data for each of the cases. The plot in (a) shows the predictions for an applied stress of $\sigma_y = -0.0125$ MPa which was the smallest possible load experimentally.¹⁷ As is expected the predicted strain based on coefficients determined from $\sigma_p = -0.0125$ MPa matches both magnitude and slope. For the coefficients determined from the $\sigma_p = -0.62$, $\sigma_p = -1.79$, and $\sigma_p = -4.16$ MPa data the strain magnitude and slope of the hysteresis kernel are underestimated with a maximum error for the $\sigma_p = -4.16$ case of about 3100 which corresponds to about a 75% error with respect to the maximum strain output. Panel (b) shows similar plots for the prediction of the strain at $\sigma_y = -0.62$ MPa. As before, the prediction based on coefficients calculated from the data collected for the same applied load case matches the data closely in both magnitude and slope and predictions based on data for higher loads underestimate both slope and magnitude of the hysteresis kernels. The maximum error for this load is found for the prediction based on the $\sigma_p = -0.0125$ MPa case and is calculated to be 2800 or about a 220% overestimation with respect to the maximum strain output. The predictions for the $\sigma_y = -1.79$ and $\sigma_y = -4.16$ MPa cases are shown respectively in panels (c) and (d). The trends established in (a) and (b) are continued with the $\sigma_p = \sigma_y$ case matching closely and $\sigma_p < \sigma_y$ cases underestimating the slopes and magnitudes of the kernel while the $\sigma_p > \sigma_y$ cases overestimate these values. In each case the maximum absolute value of the error was found for the $\sigma_p = -0.0125$ MPa case and it increases as the difference in stress levels increase being about 380% for $\sigma_y = -1.79$ MPa and about 440% for $\sigma_y = -4.16$ MPa.

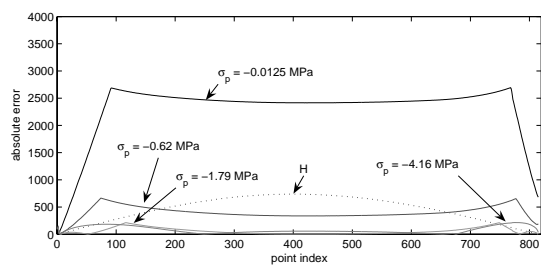
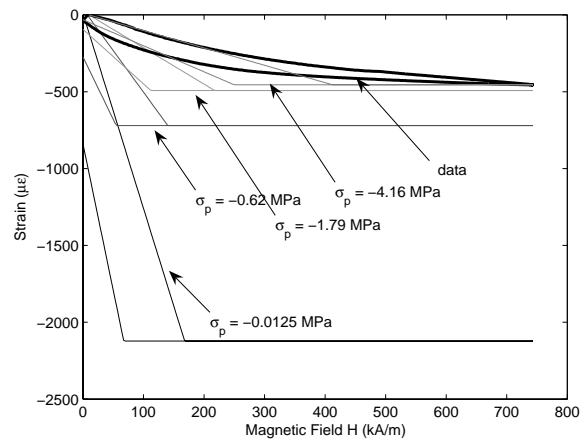
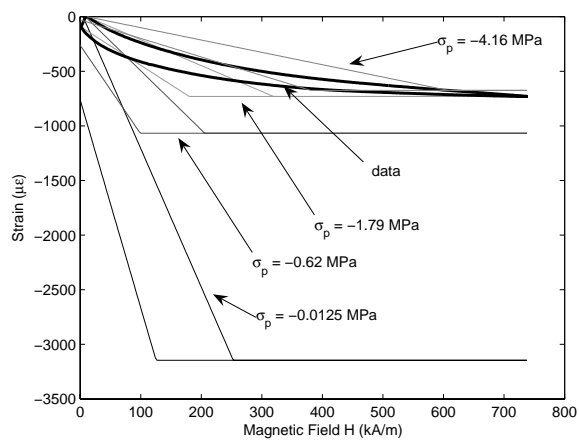
The error between the predicted and experimental outputs is quantified by various means in Table 3 where e is the absolute value of the difference between the data and the prediction for each of the 174 data points, $\sum e$ is the sum of these errors, $\langle e \rangle$ is the average value of the error, $\max(e)$ is the maximum of the error, and $e(H_{max})$ is the error at the maximum value of the field. It is observed that the two situations of largest error are (a) predictions based on parameters generated from the 0.0125 MPa data and (b) predictions for the output for the sample under 0.0125 MPa load based on parameters calculated from other data sets. As the stress levels increase, the difference in achievable strains decreases and the error correspondingly decreases. This suggests that stress ranges may need to be defined within which a specific set of parameters are appropriate and that these ranges would be smaller for lower applied stress. It is noted that, as in the model by Kiefer and Lagoudas,¹ this model accurately describes the overall trend of strain output decrease with increased load.



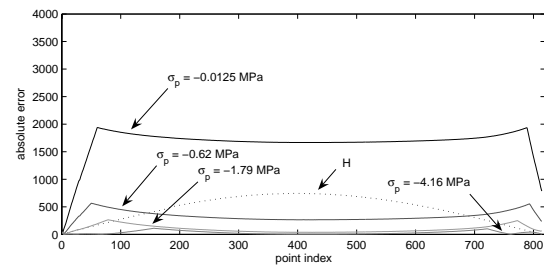
(a) $\sigma_y = -0.0125$ MPa



(b) $\sigma_y = -0.62$ MPa



(c) $\sigma_y = -1.79$ MPa



(d) $\sigma_y = -4.16$ MPa

Figure 10. Predicted strain compared with actual strain for parameters calculated from various data sets.

Table 3. Error comparison for various choices of parameter source data

	Parameter Source Data			
	$\sigma_p = -0.0125MPa$	$\sigma_p = -0.62MPa$	$\sigma_p = -1.79MPa$	$\sigma_p = -4.16MPa$
$\sigma_y = -0.0125MPa$	$\Sigma e = 186 \times 10^3$ $\langle e \rangle = 288$ $\max(e) = 849$ $e(H_{max}) = 3$	$\Sigma e = 1779 \times 10^3$ $\langle e \rangle = 2182$ $\max(e) = 2674$ $e(H_{max}) = 2673$	$\Sigma e = 2147 \times 10^3$ $\langle e \rangle = 2634$ $\max(e) = 3109$ $e(H_{max}) = 3107$	$\Sigma e = 2328 \times 10^3$ $\langle e \rangle = 2857$ $\max(e) = 3272$ $e(H_{max}) = 3179$
$\sigma_y = -0.62MPa$	$\Sigma e = 1849 \times 10^3$ $\langle e \rangle = 2269$ $\max(e) = 2754$ $e(H_{max}) = 2461$	$\Sigma e = 72 \times 10^3$ $\langle e \rangle = 88$ $\max(e) = 369$ $e(H_{max}) = 2$	$\Sigma e = 278 \times 10^3$ $\langle e \rangle = 341$ $\max(e) = 470$ $e(H_{max}) = 402$	$\Sigma e = 418 \times 10^3$ $\langle e \rangle = 513$ $\max(e) = 691$ $e(H_{max}) = 468$
$\sigma_y = -1.79MPa$	$\Sigma e = 1873 \times 10^3$ $\langle e \rangle = 2298$ $\max(e) = 2694$ $e(H_{max}) = 2416$	$\Sigma e = 325 \times 10^3$ $\langle e \rangle = 399$ $\max(e) = 664$ $e(H_{max}) = 337$	$\Sigma e = 46 \times 10^3$ $\langle e \rangle = 57$ $\max(e) = 212$ $e(H_{max}) = 0$	$\Sigma e = 64 \times 10^3$ $\langle e \rangle = 78$ $\max(e) = 215$ $e(H_{max}) = 56$
$\sigma_y = -4.16MPa$	$\Sigma e = 1354 \times 10^3$ $\langle e \rangle = 1664$ $\max(e) = 1938$ $e(H_{max}) = 1667$	$\Sigma e = 269 \times 10^3$ $\langle e \rangle = 331$ $\max(e) = 565$ $e(H_{max}) = 265$	$\Sigma e = 79 \times 10^3$ $\langle e \rangle = 97$ $\max(e) = 264$ $e(H_{max}) = 37$	$\Sigma e = 25 \times 10^3$ $\langle e \rangle = 31$ $\max(e) = 111$ $e(H_{max}) = 0$

5. STOCHASTIC HOMOGENIZATION FORMULATION

The error calculations presented in Section 4 highlight the limitations of model equation (9) as a tool to quantify the field induced strain under various external axial loads. The model errors are in part due to the simplicity of the shape chosen for the predicted curve and to the form of the equation used to fit the data in Figure 8. Errors are also due to two simplifying assumptions made in the physical description of the mechanics of the system.

1. The sample is assumed to consist of only two variants with a single boundary. In reality, however, Ni-Mn-Ga has many twin variants though only two distinct orientations. This implies that a sample will have numerous twin boundaries and thus numerous pinning sites. As discussed by Marioni¹⁴ the pinning energies vary over quite a large range which translates into a variation of the slopes k_1 and k_2 .
2. The field is assumed to be uniform throughout the sample. However, due to the short-range interactions the magnetic field in Ni-Mn-Ga can be considered to behave locally in a fashion similar to the mean field proposed by Weiss.¹⁸ Thus, the magnitude of the field at a given point in the material is not equal to the applied field but rather, is given by an effective field which is dependent on the applied field and the value of the magnetization,

$$H_e = H + H_i = H + \alpha M. \quad (10)$$

The mean field constant α varies from point to point in the material due to differences in the lattice structure.

Expression 7 quantifies the volume fraction and corresponding strain produced by an idealized single crystal which consists of two variants and is exposed to homogeneous fields. Furthermore, the pinning sites are assumed to be homogeneously distributed throughout the material. Stochastic homogenization methods like that developed by Smith^{19, 20} allow for extension of hysteresis models for ideal single crystals to more general regimes where the lattice structure and magnetic field are not homogeneous, as is the case in most engineered polycrystalline materials. For implementation, we will treat the pinning strength and interaction field as statistical distributions. This yields

$$[\xi(H, \sigma)](t) = \int_0^\infty \int_{-\infty}^\infty \nu_1(H_i) \nu_2(k_2) [\bar{\xi}(H + H_i, \sigma, k_2)](t) dH_i dk_2 \quad (11)$$

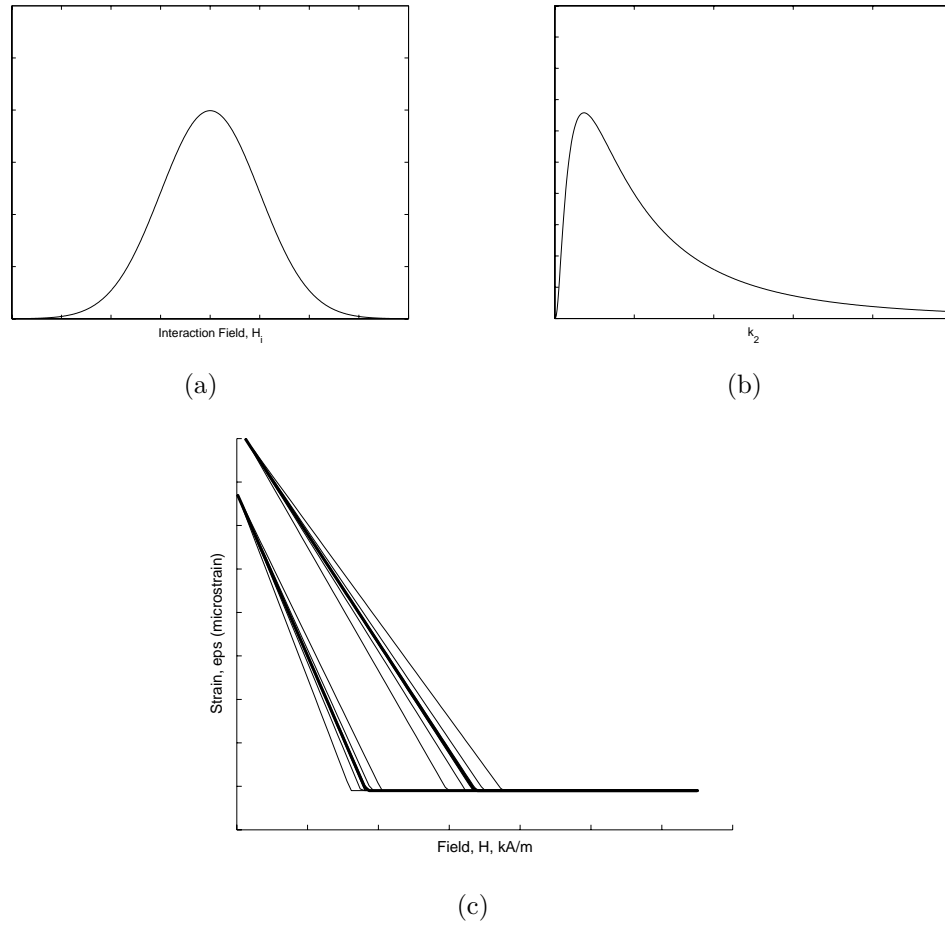


Figure 11. Distributions for (a) interaction field H_i , (b) pinning site strength k_2 and (c) the effects of the k_2 distribution on the hysteresis kernels.

where ν_1 and ν_2 are appropriately chosen distributions and $\bar{\xi}$ is given by expression (7). Since the Weiss interaction field is known to have both positive and negative values the appropriate distribution is chosen as

$$\nu_1(H_i) = c_1 e^{-H_i^2/(2b^2)} \quad (12)$$

which is a normal distribution centered at $H_i = 0$, as shown in Figure 11(a). The pinning site energies were incorporated into the energy equations as effective mechanical springs. Thus, the values for k_2 will never be negative. To meet this criterion the distribution over k_2 is chosen to be log-normal, as shown in Figure 11(b), and is given by

$$\nu_2(k_2) = c_2 e^{-\left(\ln(k_2/\bar{k}_2)/2c\right)^2}. \quad (13)$$

The effect of this distribution on the slopes of the hysteresis kernels is shown in Figure 11c.

Future efforts will focus on the application of this formulation to develop more accurate predictions of both the magnitude and shape of the hysteric strain per input field curves for various applied strain levels. Such predictions will be valuable in the design and control of solenoid based Ni-Mn-Ga transducers.

6. CONCLUSIONS

This paper has presented an adaptation to the existing theory of the internal mechanics of FMSA behavior to include the effect of pinning site energies and to explain the existence of reversible strains in $\text{Ni}_{50}\text{Mn}_{28.7}\text{Ga}_{21.3}$ when no restoring force is applied. A thermodynamic approach was used to modify the energy expressions to include the pinning energy as effective springs attached to the twin variant boundary. These mathematical expressions for the energy of the system were used to derive an expression for an idealized hysteresis kernel that predicts the strain produced by the material under various loading conditions. An error analysis for this model showed that though some basic trends were predicted the errors are too large for the model to be employed independently. A procedure was presented that will lead to more accurate strain predictions by using stochastic distributions to weight various forms of this hysteresis kernel. Future work will employ this approach in the development of more accurate models for the nonlinear, hysteric strain under various operating conditions which will allow for easier design and control of Ni-Mn-Ga solenoid transducers.

7. ACKNOWLEDGMENTS

The authors would like to express sincerest appreciation to Ralph Smith and Björn Kiefer for useful discussions and correspondence. The work of LEF is supported by a graduate fellowship from the Ohio Space Grant Consortium. The work of MJD is supported in part by NSF grant #CMS-0409512.

REFERENCES

1. B. Kiefer and D. C. Lagoudas, "Phenomenological modeling of ferromagnetic shape memory alloys," *Proceedings of SPIE Smart Structures and Materials Conf.*, **5387**, pp. 164–176, July 2004.
2. S. Murray, M. Marioni, P. Tello, S. Allen, and R. O'Handley, "Giant magnetic-field-induced strain in Ni-Mn-Ga crystals: experimental results and modeling," *Journal of Magnetism and Magnetic Materials*, **226-230**, pp. 945–947, May 2001.
3. A. Likhachev, A. Sozinov, and K. Ullakko, "Influence of external stress on the reversibility of magnetic-field-controlled shape memory effect in Ni-Mn-Ga," *Proceedings of SPIE Smart Structures and Materials Conf.*, **4333**, pp. 197–206, 2001.
4. A. Sozinov, A. Likhachev, N. Lanska, and K. Ullakko, "Giant magnetic-field-induced strain in NiMnGa seven-layered martensitic phase," *Applied Physics Letters*, **80**, pp. 1746–1748, March 2002.
5. L. E. Faidley, M. J. Dapino, G. N. Washington, and T. A. Lograsso, "Dynamic response in the low-kHz range and Delta-E effect in ferromagnetic shape memory Ni-Mn-Ga," *Proceedings of IMECE 2003* (43198), 2003.
6. R. C. O'Handley, S. Murray, M. A. Marioni, H. Nembach, and S. Allen, "Phenomenology of giant magnetic-field induced strain in ferromagnetic shape-memory materials," *J. Appl. Phys.*, **87**, pp. 4712–4717, May 2000.
7. R. Tickle and R. James, "Magnetic and magnetomechanical properties of $\text{Ni}_{52}\text{Mn}_{48}\text{Ga}$," *Journal of Magnetism and Magnetic Materials (Netherlands)*, **195**, pp. 627–638, June 1999.
8. A. Likhachev and K. Ullakko, "Magnetic-field-controlled twin boundaries motion and giant magneto-mechanical effects in Ni-Mn-Ga shape memory alloy," *Physics Letters A*, , pp. 142–151, October 2000.
9. S. Murray, M. Marioni, S. Allen, R. O'Handley, and T. Lograsso, "6% magnetic-field-induced strain by twin-boundary motion in ferromagnetic Ni-Mn-Ga," *Applied Physics Letters*, **77**(6), pp. 886–888, 2000.
10. R. Tickle, *Ferromagnetic Shape Memory Materials*. PhD thesis, Texas A&M, 2000.
11. K. Ullakko, "Magnetically controlled shape memory alloys: A new class of actuator materials," *Journal of Materials Engineering and Performance*, **5**, pp. 405–409, June 1996.
12. L. Faidley, M. Dapino, G. Washington, and T. Lograsso, "Dynamic behavior and stiffness tuning in solenoid based Ni-Mn-Ga transducers," *Proceedings of SPIE Smart Structures and Materials Conf.*, , March 2004.
13. A. Malla, "Effect of composition of the magnetic and elastic properties of shape memory Ni-Mn-Ga," Master's thesis, The Ohio State University, June 2003.
14. M. A. Marioni, S. M. Allen, and R. C. O'Handley, "Nonuniform twin-boundary motion in Ni-Mn-Ga single crystals," *Applied Physics Letters*, **84**, pp. 4071 – 4073, May 2004.

15. R. M. Bozorth, *Ferromagnetism*, D. Van Nostrand Company, Inc, New York, 1951.
16. R. C. Smith, *Smart Material Systems: Model Development*, Society for Industrial & Applied Mathematics, Philadelphia, PA, in print.
17. A. Malla, M. Dapino, and T. Lograsso, "Effect of composition on the magnetic and elastic properties of shape memory NiMnGa," *Proceedings of SPIE Smart Structures and Materials Conf.* , March 2003.
18. D. Jiles, *Magnetism and Magnetic Materials*, Chapman & Hall, 1995.
19. R. C. Smith, S. Seelecke, M. J. Dapino, and Z. Ounaies, "A unified model of hysteresis in ferroic materials," *Proceedings of SPIE Smart Structures and Materials Conf.* **5049**, pp. 88–99, March 2003.
20. R. C. Smith and J. E. Massad, "A unified methodology or modeling hysteresis in ferroelectric, ferromagnetic, and ferroelastic materials," Tech. Rep. CRSC-TR01-10, CRSC, NC State, April 2001.